Manuscript number: WW/2004/022485

Hydrodynamic Characteristics of Pile-Supported Vertical Wall Breakwaters

By Kyung-Duck Suh, A.M.ASCE[1], Sungwon Shin, S.M.ASCE[2], and Daniel T. Cox, M.ASCE[3]

Abstract: This paper describes the hydrodynamic characteristics of a pile-supported vertical wall breakwater, the upper part of which is a vertical wall and the lower part consists of an array of vertical piles. For regular waves, using the eigenfunction expansion method, a numerical model has been developed that can compute wave transmission, reflection, and runup, and wave force acting on the breakwater. For irregular waves, the regular wave model is repeatedly used for each frequency component of the irregular wave spectrum. The wave period is determined according to the frequency of the component wave, while the root-mean-squared wave height is used for all the component waves to compute the energy dissipation between piles. To examine the validity of the developed models, large-scale laboratory experiments have been conducted for pile-supported vertical wall breakwaters with a constant spacing between piles but various drafts of the upper vertical wall. Comparisons between measurement and prediction show that the numerical model adequately reproduces most of the important features of the experimental results for both regular and irregular waves. The pile-supported vertical wall breakwater always gives smaller transmission and larger reflection than a curtain wall breakwater with the same draft as that of the upper wall, or a pile breakwater with the same porosity as that of the lower part, of the pile-supported vertical wall breakwater.

---

[1] Professor, School of Civil, Urban and Geosystem Engineering, Seoul National University, San 56-1, Shinlim-Dong, Gwanak-Gu, Seoul 151-742, Korea. E-mail: kdsuh@snu.ac.kr

[2] Graduate Student, Department of Civil, Construction, and Environmental Engineering, Oregon State University, 202 Apperson Hall, Corvallis, OR 97331-2302, USA. E-mail: shinsu@engr.orst.edu

[3] Associate Professor, Department of Civil, Construction, and Environmental Engineering, Oregon State University, 202 Apperson Hall, Corvallis, OR 97331-2302, USA. E-mail: Dan.Cox@oregonstate.edu

Keywords: Breakwaters; Laboratory experiments; Numerical models; Piles; Wave force; Wave reflection; Wave runup; Wave transmission.

Introduction

Gravity-type breakwaters using rubble mound or vertical caissons have been widely used to provide a calm basin for ships and to protect harbor facilities from rough seas. In general, the width of these breakwaters increases with water depth, leaving a large footprint and requiring a great amount of construction material especially when built in deeper water. Often they block littoral drift and cause severe erosion or accretion in neighboring beaches. In addition, they prevent the circulation of water and so deteriorate the water quality within the harbor. In some places, they obstruct the passage of fishes and bottom dwelling organisms. A solid soil foundation is also needed to support such heavy structures.

In order to resolve the above-mentioned problems, porous (permeable) structures have been introduced especially in small craft harbors. The simplest porous structure may be a curtain wall breakwater (sometimes called wave screen or skirt breakwater), which consists of a vertical wall extending from the water surface to some distance above the seabed (Wiegel 1960; Kriebel and Bollmann 1996; Kriebel et al. 1998). Recently Isaacson et al. (1998) proposed a slotted curtain wall breakwater. Another simple porous structure may be an array of vertical piles, which is called a pile breakwater in this study. The closely spaced piles induce energy dissipation due to the viscous eddies formed by the flow through the gaps. To examine the wave scattering by vertical piles, hydraulic model tests have been used (e.g., Hayashi et al. 1966; Kojima et al. 1988; Uda et al. 1990; Kakuno and Liu 1993). Efforts towards developing analytical models to calculate the reflection and transmission coefficients have also been made (e.g., Kakuno and Liu 1993; Hagiwara 1984; Bennett et al. 1992; Park et al. 2000).

In this paper, we deal with a pile-supported vertical wall breakwater, the upper part of which is a vertical wall and the lower part consists of an array of vertical piles. For short waves in which the wave motion is minimal in the lower part of the water column, this breakwater would behave like a conventional curtain wall breakwater, while for longer waves additional energy dissipation would occur due to flow separation around the piles, giving less wave transmission than the conventional curtain wall breakwater. In

comparison with a pile breakwater, we expect somewhat smaller transmission for long waves and much smaller transmission for short waves because the upper part of the breakwater is blocked by a vertical wall. The purpose of the present paper is to develop a numerical model to compute various hydrodynamic characteristics of a pile-supported vertical wall breakwater, to describe the large-scale laboratory experiment performed to assess the numerical model, and finally to compare the predictions of the model with the experimental results.

Numerical Model

Boundary Value Problem

Let us consider the pile-supported vertical wall breakwater sketched in Fig. 1, in which h = constant water depth in still water; d = height of the impermeable wall below the still water level; b = thickness of the wall. A Cartesian coordinate system (x,z) is defined with the positive x directing downwave from the crest line of the breakwater and the vertical coordinate z being measured vertically upwards from the still water line. The distance between the centers of two neighboring piles is denoted as $2A$ and the width of an opening is $2a$ so that the porosity of the lower part of the breakwater at $x=0$ is defined as $r_0 = a/A$. A regular wave train with wave height H_i is incident in the positive x-direction. We divide the fluid domain into region 1 ($x \le 0$) and region 2 ($x \ge 0$).

Assuming incompressible fluid and irrotational flow motion, the velocity potential exists, which satisfies the Laplace equation. Linearizing the free-surface boundary conditions, the following boundary value problem for the velocity potential $\Phi(x,z,t)$ is obtained:

$$\frac{\partial^2 \Phi}{\partial x^2} + \frac{\partial^2 \Phi}{\partial z^2} = 0 \tag{1}$$

$$\frac{\partial \Phi}{\partial z} - \frac{\omega^2}{g}\Phi = 0 \qquad \text{at} \quad z = 0 \tag{2}$$

$$\frac{\partial \Phi}{\partial z} = 0 \qquad \text{at} \quad z = -h \tag{3}$$

where ω = wave angular frequency; and g = gravitational acceleration. Assuming periodic motion in time t, we can assume the solution to the above problem as

$$\Phi(x,z,t) = \mathrm{Re}\left\{-\frac{igH_i}{2\omega}\frac{1}{\cosh(kh)}\phi(x,z)\exp(-i\omega t)\right\} \tag{4}$$

where $i=\sqrt{-1}$; and the symbol Re represents the real part of a complex value. The wave number k must satisfy the dispersion relationship, $\omega^2 = gk\tanh(kh)$. The spatial variation of the velocity potential $\phi(x,z)$ should be determined in each region.

We assume that the length scale of the flow near the breakwater is of the order of the wall thickness, which is much smaller than the far-field length scale of $O(k^{-1})$, so that the wall has no thickness mathematically and the three-dimensional feature near the breakwater does not significantly affect the two-dimensional far-field solutions. Then $\phi_1(x,z)$ and $\phi_2(x,z)$ must satisfy the following matching conditions at $x=0$:

$$\frac{\partial\phi_1}{\partial x} = \frac{\partial\phi_2}{\partial x} = 0 \qquad \text{for} \quad -d \le z \le 0, \quad x=0 \tag{5}$$

$$\frac{\partial\phi_1}{\partial x} = \frac{\partial\phi_2}{\partial x} = iG(\phi_1-\phi_2) \qquad \text{for} \quad -h \le z \le -d, \quad x=0 \tag{6}$$

where the subscripts indicate the regions of the fluid domain. The first matching condition describes that the horizontal velocities vanish on both sides of the upper impermeable wall of the breakwater. The second one for the lower part of the breakwater describes that the horizontal mass fluxes (or indirectly horizontal velocities) in the two regions must be same at the breakwater and that the horizontal velocity at the opening is proportional to the difference of velocity potentials, or the pressure difference, across the breakwater. The proportional constant G, often called permeability parameter, is in general complex. There are several ways to express the constant G (see Isaacson et al. 1998). In the present study, we adopt the method of Mei et al. (1974) and G is expressed by

$$G = \frac{1}{\frac{\beta}{\omega} - i\ell} \tag{7}$$

where β = energy dissipation coefficient derived by linearizing the nonlinear convective acceleration term in the equation of motion; and ℓ = length of the jet flowing through the gap between piles. The real part of the denominator in Eq. (7) corresponds to the resistance of the barrier and the imaginary part is associated with the phase difference between the velocity and the pressure due to inertial effects.

The linearized dissipation coefficient β is given by Kim (1998) as

$$\beta = \frac{8\alpha}{9\pi} H_i \omega \frac{1}{\sqrt{(R+2)^2 + P^2}} \frac{5 + \cosh(2kh)}{2kh + \sinh(2kh)} \tag{8}$$

where $P = \ell k$; $R = \beta k / \omega$; and α = head loss coefficient. The preceding equation was derived for a pile breakwater without a vertical wall. However, it could be used for a pile-supported vertical wall breakwater because the mechanism of energy dissipation between piles must be similar for these two breakwaters. A pile breakwater has energy dissipation associated with the free surface, but it is assumed to be small compared with the energy dissipation between piles. Rearrangement of Eq. (8) gives a quartic polynomial of β, which can be solved by the eigenvalue method (e.g., Press et al. 1992).

Suh et al. (2002) showed that the jet length ℓ is related to the blockage coefficient C by

$$\ell = 2C \tag{9}$$

Kakuno and Liu (1993) proposed the blockage coefficient as

$$C = \frac{b}{2}\left(\frac{1}{r_0} - 1\right) + \frac{2A}{\pi}\left[1 - \log(4r_0) + \frac{1}{3}r_0^2 + \frac{281}{180}r_0^4\right] \tag{10}$$

for rectangular piles. The head loss coefficient α could be given by the plate orifice formula (Mei 1983):

$$\alpha = \left(\frac{1}{r_0 C_c} - 1 \right)^2 \tag{11}$$

where C_c = empirical contraction coefficient, for which Mei et al. (1974) suggested using the formula:

$$C_c = 0.6 + 0.4 r_0^2 \tag{12}$$

The above method to compute the permeability constant is advantageous compared with other methods in that all the related parameters are known; i.e. incident wave height and period and the geometrical parameters of the barrier. In the method of Isaacson et al. (1998), for example, the values of friction and added mass coefficients are not known *a priori* and they are estimated on the basis of a best fit between measurement and prediction.

Eigenfunction Expansion Method

To solve the boundary value problem, Eqs. (1) to (3), we use the eigenfunction expansion method. We closely follow the method of Isaacson et al. (1998), in which the velocity potential is expressed in a series of infinite number of solutions:

$$\phi_1 = \phi_i - \sum_{m=0}^{\infty} A_m \cos[\mu_m (h+z)] \exp(\mu_m x) \tag{13}$$

$$\phi_2 = \phi_i + \sum_{m=0}^{\infty} A_m \cos[\mu_m (h+z)] \exp(-\mu_m x) \tag{14}$$

where $\phi_i = \cosh[k(h+z)]\exp(ikx)$ is the incident wave potential. The wave numbers

μ_m are the solution of the dispersion relation, $\omega^2 = -g\mu_m \tan(\mu_m h)$, which has an infinite discrete set of real roots $\pm\mu_m$ ($m \geq 1$) for non-propagating evanescent waves and a pair of imaginary roots $\mu_0 = \pm ik$ for propagating waves. We take $\mu_0 = -ik$ so that the propagating waves in Eqs. (13) and (14) correspond to reflected and transmitted waves, respectively. We also take the positive roots for $m \geq 1$ so that the non-propagating waves die out exponentially with the distance from the breakwater.

Now the solutions (13) and (14) satisfy the free surface boundary condition (2) and the bottom boundary condition (3). Also, they automatically satisfy the requirement that the horizontal velocities must be matched at the breakwater. In order to solve for the unknown coefficients A_m's, we use the matching conditions at the breakwater. First, Eqs. (13) and (14) are substituted into Eq. (5) and (6), respectively. Multiplying each resulting equation by $\cos[\mu_n(h+z)]$, integrating with respect to z over the appropriate domain of z (i.e., $z=-d$ to 0, or $z=-h$ to $-d$), and finally adding them, we obtain a matrix equation for A_m:

$$\sum_{m=0}^{\infty} C_{mn} A_m = b_n \quad \text{for } n = 0,1,2,\cdots,\infty \tag{15}$$

where

$$C_{mn} = \mu_m f_{mn}(-d,0) + (\mu_m - 2iG) f_{mn}(-h,-d) \tag{16}$$

$$b_n = -\mu_0 \left[f_{0n}(-d,0) + f_{0n}(-h,-d) \right] \tag{17}$$

$$f_{mn}(p,q) = \int_p^q \cos[\mu_m(h+z)]\cos[\mu_n(h+z)]dz$$

$$= \begin{cases} \dfrac{1}{2}\left[\dfrac{\sin[(\mu_m+\mu_n)(h+z)]}{\mu_m+\mu_n} + \dfrac{\sin[(\mu_m-\mu_n)(h+z)]}{\mu_m-\mu_n} \right]_p^q & \text{for } m \neq n \\ \dfrac{1}{4\mu_{\mathrm{m}}} \left[2\mu_m(h+z) + \sin[2\mu_m(h+z)] \right]_p^q & \text{for } m = n \end{cases} \tag{18}$$

Note that the numerical model developed for a pile-supported vertical wall breakwater in this study can be used for a pile breakwater just by setting $d = 0$. It can also be used for a curtain wall breakwater by changing the permeability parameter in Eq.

(7) to $G = 1/b$, which was derived from the energy dissipation formula for a curtain wall breakwater of Kriebel (2000).

Engineering Wave Properties

Once the wave potentials are calculated, we can obtain various engineering wave properties. The reflection and transmission coefficients are given by

$$C_r = |A_0| \tag{19}$$

and

$$C_t = |1 + A_0| \tag{20}$$

respectively. The energy loss coefficient, which is the portion of the incident wave energy that is dissipated by the breakwater, is given by

$$C_l = 1 - C_r^2 - C_t^2 \tag{21}$$

The wave runup on the upwave face of the breakwater is given by

$$R_u = \frac{H_i}{2}\left|1 - \frac{1}{\cosh(kh)}\sum_{m=0}^{\infty} A_m \cos(\mu_m h)\right| \tag{22}$$

In the limiting case of a full-depth impermeable vertical wall ($d \to h$ or $r_0 \to 0$), $A_m = 0$ for all $m \geq 1$ and $A_0 = -1$ so that $C_r = 1.0$, $C_t = 0.0$, and $R_u = H_i$ as expected.

Since the vertical distributions of wave pressure on both upwave and downwave sides of the breakwater are known, the wave force can also be calculated. The maximum

horizontal wave force $F_{\max}$ per unit width of the breakwater are given by

$$F_{\max} = \rho g H_i \frac{1}{\cosh(kh)} \left| \sum_{m=0}^{\infty} \frac{A_m}{\mu_m} \{\sin(\mu_m h) - r_0 \sin[\mu_m (h-d)]\} \right| + \frac{\rho g}{8} H_i^2 \left\{ \left[1 - \frac{1}{\cosh(kh)} \sum_{m=0}^{\infty} A_m \cos(\mu_m h) \right]^2 - \left[1 + \frac{1}{\cosh(kh)} \sum_{m=0}^{\infty} A_m \cos(\mu_m h) \right]^2 \right\} \quad (23)$$

where ρ = density of fluid. The second term on the right hand side represents the second-order force contribution of the wave crest regions on the upwave and downwave sides of the breakwater (Dean and Dalrymple, 1991). Without this term, in the limiting case of a full-depth impermeable vertical wall ($d \to h$ or $r_0 \to 0$), $A_m = 0$ for all $m \geq 1$ and $A_0 = -1$ so that the preceding equation becomes

$$F_{\max}^s = \rho g H_i \frac{1}{k} \frac{\sinh(kh)}{\cosh(kh)} \quad (24)$$

where the superscript s stands for the standing wave in front of an impermeable vertical wall. In another limiting case of no breakwater ($d \to 0$ and $r_0 \to 1$), $F_{\max}$ becomes zero as expected.

Extension to Irregular Waves

Using the above regular wave model, the reflection and transmission coefficients can be calculated differently for each frequency component, i.e., $C_r(f)$ and $C_t(f)$ where f = wave frequency. In the computation of the energy dissipation coefficient β in Eq. (8), the root-mean-squared (abbreviated as rms hereafter) wave height is used in place of the incident wave height H_i, because the flow separation due to irregular waves and the resulting energy dissipation are induced not by the individual component waves but by the superposition of the component waves. The spectral densities of the reflected and transmitted waves, respectively, are calculated for a particular frequency component by

$$S_{\eta,r}(f) = \left|C_r(f)\right|^2 S_{\eta,i}(f) \tag{25}$$

$$S_{\eta,t}(f) = \left|C_t(f)\right|^2 S_{\eta,i}(f) \tag{26}$$

where $S_{\eta,i}(f)$ = incident wave energy density. The corresponding energy loss spectrum is given by

$$S_{\eta,l}(f) = \left\{1 - \left|C_r(f)\right|^2 - \left|C_t(f)\right|^2\right\} S_{\eta,i}(f) \tag{27}$$

The frequency-averaged reflection and transmission coefficients are then calculated as (Goda, 2000)

$$\overline{C_r} = \sqrt{\frac{m_{0,r}}{m_{0,i}}} \tag{28}$$

$$\overline{C_t} = \sqrt{\frac{m_{0,t}}{m_{0,i}}} \tag{29}$$

where $m_{0,i}$, $m_{0,r}$, and $m_{0,t}$ = zeroth moments of the incident, reflected, and transmitted wave spectra, respectively. Note that the reflection and transmission coefficients calculated by the conventional method, as the ratio of the reflected and transmitted rms wave heights to the incident one, are equivalent to the frequency-averaged coefficients because the rms wave height is proportional to $\sqrt{m_0}$. The corresponding frequency-averaged energy loss coefficient is given by

$$\overline{C_l} = \frac{m_{0,l}}{m_{0,i}} \tag{30}$$

where $m_{0,l}$ = zeroth moment of energy loss spectrum.

The force spectrum, $S_F(f)$, is calculated by

$$S_F(f) = |T_F(f)|^2 S_{\eta,i}(f) \tag{31}$$

where $T_F(f)$ is the frequency-dependent transfer function between wave amplitude and force amplitude, which can be computed by using the linear term in Eq. (23) as

$$T_F = 2\rho g \frac{1}{\cosh(kh)} \sum_{m=0}^{\infty} \frac{A_m}{\mu_m} \{\sin(\mu_m h) - r_0 \sin[\mu_m (h-d)]\} \tag{32}$$

The zero-moment force, F_{m0}, can then be determined as

$$F_{m0} = 2\left[\int_0^{\infty} S_F(f) df\right]^{1/2} \tag{33}$$

Note that a factor of 2 instead of 4 was used in order to represent the force amplitude. The dimensionless zero-moment force, $\hat{F}_{m0}$, is defined as

$$\hat{F}_{m0} = \frac{F_{m0}}{F_{m0}^s} \tag{34}$$

In this expression, the normalizing quantity is the zero-moment force predicted on a full-depth vertical wall based on linear wave theory as

$$F_{m0}^{s} = \rho g H_s \frac{\tanh(k_p h)}{k_p} \tag{35}$$

where H_s = significant wave height, and k_p = wave number associated with the peak frequency of the incident wave spectrum. The significant wave height is calculated by

$$H_s = c_1 \sqrt{m_{0,i}} \tag{36}$$

where c_1 = 3.83, 3.87, and 3.91 for the peak enhancement factor of the JONSWAP spectrum γ = 1, 3.3, and 10, respectively. On the other hand, the spectral peak period is calculated by

$$T_p = \frac{1}{c_2} \sqrt{m_{0,i} / m_{2,i}} \tag{37}$$

where $m_{2,i}$ = second moment of the incident wave spectrum, and c_2 = 0.71, 0.78, and 0.85 for γ = 1, 3.3, and 10, respectively (Goda, 2000).

Large-Scale Laboratory Experiment

Experiments were carried out in the large wave flume at the O.H. Hinsdale Wave Research Laboratory of Oregon State University. Fig. 2 shows the arrangement of the model breakwater and measuring instruments. The flume was 104-m long, 3.7-m wide, and 4.6-m deep. It was equipped with a hinge-type wave generator at one end, and a 1/12 sloping beach at the other. A false floor with a 1/6 fore-slope was installed at the elevation of 0.84 m from the bottom of the flume. The breakwater model was placed at a distance of 37.3 m from the wave maker and 16.2 m from the beginning of the flat false floor. Water surface displacements were measured with parallel-wire resistance-type wave gauges. Four load cells were used to measure the wave force acting on the

breakwater.

A rigid aluminum alloy frame, which shows black in Fig. 3, was used to contain the breakwater model made of wood. A vertical support for the model structure was provided by an overhead steel frame, which spanned the width of the wave flume. Steel cables extending from the overhead frame were shackle-connected to the top member of the load frame. The load frame was lifted slightly from the bottom so that the vertical load was completely supported by the cables. To measure the horizontal force acting on the breakwater, the load frame was attached to the sidewalls at four points (top and bottom on each side of the flume) by load cells that were instrumented with strain gages, as shown in Fig. 3. In this figure, two acoustic-Doppler velocimeters are also shown, which were installed to measure the water particle velocities for another project; one behind a gap and the other behind a pile.

All experiments were conducted at a water depth of 2.4 m on the false floor. Square piles were used, with a = 7.15 cm, A = 14.3 cm, and b = 14.3 cm, so that the porosity of the lower perforated wall was 0.5. Three different drafts of the upper solid wall were used; 48, 96, and 144 cm. The solid wall was high enough above the water level to prevent wave overtopping.

Regular Wave Tests

Five different wave periods (T = 1.5, 2.0, 2.5, 3.0, 4.0 s) were used with specified wave heights corresponding to a constant wave steepness, $H / L = 0.03$. The measured values of the incident wave heights and periods are given in Table 1, along with the transmission and reflection coefficients, runup, and wave forces.

To measure the incident and reflected waves, three wave gauges were installed as shown in Fig. 2. The free surface displacements measured at WG1 to WG3 were used to separate the incident and reflected waves using the technique developed by Suh et al. (2001). Wave measurements were made for 120 s at a sampling rate of 50 Hz immediately after the initiation of wave generation. For the separation of incident and reflected waves, the wave records should include the incident waves and the reflected waves from the breakwater, but not the re-reflected waves from the wave paddle. By examining the plotted wave records and using the approximate arrival time of the first reflected wave, we selected a fraction of the wave records, with a length of several wave

periods, including only the incident waves and the reflected waves from the breakwater. This was then used for the separation of incident and reflected waves. The transmitted waves were measured using one wave gage at WG4 in Fig. 2 assuming that the wave reflection from the downwave beach is negligible. Previous observations indicated reflection coefficients from the beach of 0.05 to 0.1 for the wave periods used in these tests.

Irregular Wave Tests

Irregular waves were generated from JONSWAP spectra, having peak enhancement factor of 3.3, although 1 and 10 were also used for the case of the draft of the upper wall of 96 cm. Five different peak wave periods (T_p = 1.5, 2.0, 2.5, 3.0, 4.0 s) were used with specified significant wave heights corresponding to a constant wave steepness, $H_s / L_p = 0.03$, where L_p = wavelength associated with the spectral peak period. This resulted in a total of 25 test cases. The measured values of the incident significant wave heights and peak periods are given in Tables 2, along with the measured and predicted reflection and transmission coefficients and wave forces. In this table, the superscripts m and p indicate measurement and prediction, respectively.

For irregular waves, measurements were made for 780 seconds at a sampling rate of 50 Hz immediately after the initiation of wave generation. For spectral analysis, we used 32,768 data after skipping the first 60 seconds. The time series was corrected by applying a 10% cosine taper on both ends and was subject to spectral analysis. The raw spectrum was running-averaged twice over 15 neighboring frequency bands, the total number of degrees of freedom of the final estimates being 225.

The effects of wave steepness were examined in a separate set of tests for both regular and irregular waves. In general, increasing wave steepness lead to a reduction in wave reflection, transmission, runup, and force, and consequently an increase in the energy loss at the breakwater. However, the effects of wave steepness were not so significant that the results are not presented in this paper.

Comparison with Experimental Results

In this section, the numerical results are compared with the experimental results. The number of terms used in the eigenfunction expansion method was 50, which was found to give accurate results over the range of values presented here.

Regular Waves

Fig. 4 compares the measured and predicted transmission, reflection, and energy loss coefficients as functions of kh. In general, the numerical model adequately reproduces most of the important features of the experimental results. The transmission and reflection coefficients, respectively, decrease and increase with the relative water depth. As the draft of the upper wall increases, the transmission coefficient decreases while the reflection coefficient increases, as expected. Differences between the measured and predicted results are most notable in the energy loss coefficients. Note that the measured energy loss coefficient is calculated directly from the measured transmission and reflection coefficients so that the scatter in the measured values is due in part to experimental errors in measuring the transmitted and reflected waves. As the relative water depth decreases, the predicted transmission coefficient increases to a certain maximum value and then decreases as the relative depth further decreases. The opposite trend is observed for the reflection coefficient. These trends for small kh are definitely wrong because in the limit of long waves the breakwater is invisible to the waves so that complete transmission of the waves should occur. One reason for these trends may be an incorrect behavior of β in Eq. (8) for long waves. As kh goes to zero, β goes to infinity, indicating complete dissipation of the long waves. It is difficult to define the range of applicability of Eq. (8), though the results in Fig. 4 suggest that it may be applicable for kh larger than 1.0. The experimental data were collected in the range of kh larger than about 0.8. Therefore, the numerical results will be presented for the same range hereafter.

Fig. 5 compares the measured and predicted wave runup on the upwave face of the breakwater as functions of kh. The wave runup was normalized with respect to the incident wave height. In Fig. 5(a), the measured runup is the maximum height of the water level above the still water level at the breakwater, denoted as $R_u^{(1)}$ in this paper.

The measured runup is in general larger than the model prediction probably due to the nonlinear effects, which give more peaked wave crest and flatter trough than the linear sinusoidal wave form. Since the numerical model used in this study is a linear model, it may be more reasonable to use the wave runup defined as one half of the vertical distance between the wave crest and the trough at the breakwater, denoted as $R_u^{(2)}$ in this paper. Fig. 5(b) shows a comparison using the second definition of wave runup and shows that it gives better agreement with the predictions. The normalized runup for both the measurements and predictions are greater than 1.0 for shorter waves even though the lower part of the breakwater is perforated, which is known to be 1.0 for a full-depth impermeable vertical wall. This is due to the inclusion of the evanescent waves. Without these, the normalized runup would be always smaller than 1.0 and converge to 1.0 as kh increases.

Fig. 6 compares the measured and predicted wave force acting on unit width of the breakwater as functions of kh. The wave force was normalized with respect to that on a full-depth impermeable vertical wall, $F_{\max}^s$, given by Eq. (24). A reasonably good agreement is shown between measurement and prediction, especially in the case of the smallest d/h where the wave force is relatively small. Note that, differently from the runup, the nonlinear effect was partially retrieved in the calculation of the wave force.

Careful examination of Figs. 4 to 6 shows that the disagreement between measurement and prediction is prominent in the cases of the largest and the smallest kh. In the case of the largest kh, the wave height is so small that a small measurement error could easily be exaggerated. On the other hand, in the case of the smallest kh, the wave propagates so fast that the small leading waves reflected from the breakwater could be re-reflected from the wave paddle and arrive at the wave gauges before a steady wave train is formed at the gauges. The group velocity of the wave of the period of 4 s in water depth of 2.4 m is 3.56 m/s so that it takes about 5 wave periods for the first wave passing the wave gauge to be reflected from the breakwater, re-reflected from the wave paddle, and to arrive at the gauge. According to the measured wave profiles, it takes about 4 wave periods for the wave train to reach a steady state. Because the wave records for the first 2 or 3 wave periods in the steady state were used for the separation of incident and reflected waves, there is possibility for the wave records to be contaminated by the re-

reflected waves from the wave paddle.

Irregular Waves

Figs. 7 to 9 compare the measured and predicted frequency-averaged transmission and reflection coefficients and dimensionless zero-moment force, respectively. Reasonable agreements are shown between measurement and prediction, though the numerical model somewhat over-predicts them, especially at larger values. The transmission coefficient decreases with d/h, while the reflection coefficient and wave force increase with d/h, as expected.

Fig. 10 compares the measured and predicted frequency-averaged transmission and reflection coefficients and dimensionless zero-moment force as functions of $k_p h$. The results in this figure and the following several figures differ somewhat from those in Figs. 7 to 9, in that the predicted values are determined from an idealized incident JONSWAP spectrum rather than from a measured incident spectrum. This permits the predicted results to be plotted as a smooth curve for a wide range of values of $k_p h$. In the calculation of the theoretical curves, $\gamma = 3.3$ was used. The variations with respect to the relative water depth are quite similar to those of the regular waves in Figs. 4 and 6. In general, the numerical model adequately reproduces most of the important features of the experimental results. Again the numerical results show slight over-prediction as in Figs. 7 to 9.

Fig. 11 compares the measured and predicted frequency-averaged transmission and reflection coefficients and dimensionless zero-moment force as functions of $k_p h$, for different peak enhancement factors. In the calculation of the theoretical curves, $d/h = 0.4$ was used. Both measurement and prediction show that a broader spectrum gives less transmission and more reflection in relatively shallow intermediate-depth water, where a broad spectrum has more high-frequency energy than a narrow spectrum. The reverse occurs in deeper water, where almost all high-frequency energy is reflected and a broad spectrum has more low-frequency energy than a narrow spectrum. A broader spectrum exerts less wave force in relatively deep intermediate-depth water and in deep

water, where the high-frequency component waves of the broad spectrum exert the wave force only on the upper part of the breakwater.

Now, selected comparisons of measured and predicted wave and force spectra are given in Figs. 12 to 16. In each figure, the measured incident wave spectrum, normalized by the peak energy density, is shown in the upper left panel. The remaining panels give the measured (solid line) and predicted (dashed line) spectra for transmitted waves, reflected waves, and wave forces. The transmitted and reflected wave spectra are normalized by the peak energy density of the incident spectrum, while the force spectra are normalized by the peak of the measured force spectrum. All spectra are plotted as a function of the normalized frequency, f / f_p, where $f_p = 1/T_p$ is the peak frequency of the incident wave spectrum.

Figs. 12 to 14 compare results for the broad, ordinary, and narrow wave spectra, having the peak enhancement factors of 1, 3.3, and 10, respectively. The wave conditions in Fig. 12 were T_p = 2.70 s and H_s = 25.0 cm, and those in Fig. 13 were T_p = 2.62 s and H_s = 24.1 cm, while conditions in Fig. 14 were T_p = 2.62 s and H_s = 27.3 cm. All three of these tests used d/h = 0.4. In all the cases shown, it is seen that the predicted spectra are in generally good agreement with the measured spectra. As with the frequency-averaged transmission and reflection coefficients and the dimensionless zero-moment force shown in Figs. 7 to 9, the numerical model somewhat over-predicts wave transmission, reflection and force, especially near the peak of the spectrum. The peak frequency calculated by Eq. (37) is slightly smaller than the frequency corresponding to the peak energy density because the measured incident wave spectrum somehow has less energy density than the theoretical spectrum in the high frequency region.

For the experimental results presented in Table 2, the relative errors of the numerical model were calculated by

$$\text{Error} = \frac{A^p - A^m}{A^p} \times 100\% \tag{38}$$

where A denotes any experimental variable, i.e., $\overline{C_t}$, $\overline{C_r}$, or $\hat{F}_{m0}$. Fig. 15 shows the results for the case of $d/h = 0.2$, $\gamma = 3.3$, T_p = 3.75 s, and H_s = 49.7 cm, for which the average of the absolute values of the relative errors was the smallest as 7.2%, i.e., the most error-free. The numerical model under-predicts the wave transmission throughout the frequency, while it over- or under-predicts the wave reflection and force depending on the frequency. As a whole, however, the numerical model predicts the frequency-dependent nature of the wave characteristics quite well.

Fig. 16 shows the results for the case of $d/h = 0.4$, $\gamma = 10.0$, T_p = 1.63 s, and H_s = 9.4 cm, for which the average of the absolute values of the relative errors was the greatest as 36.5%. The predicted energy density of transmitted waves is very small throughout the frequency, showing several spikes, but the agreement is excellent for the wave reflection and force. In this case, the transmitted wave energy is so small that a small measurement error could easily be exaggerated.

A pile-supported vertical wall breakwater permits less wave transmission than a conventional curtain wall breakwater because additional energy dissipation occurs due to flow separation around the piles. It also gives less transmission than a pile breakwater because the upper part is blocked by a vertical wall. Fig. 17 shows a comparison of frequency-averaged transmission, reflection, and energy loss coefficients among these three types of breakwaters as functions of $k_p h$. The computational conditions for the pile-supported vertical wall breakwater were the same as the previous experimental conditions, with $d/h = 0.4$ and $\gamma = 3.3$. For the curtain wall breakwater, just the piles were removed, and the energy dissipation below the vertical wall was calculated using the model of Kriebel (2000). For the pile breakwater, the upper wall was removed and the piles were extended to the water surface. As expected, the difference between the first two types of breakwater is small in deep water but it becomes prominent as approaching shallow water. On the other hand, the difference between the pile-supported vertical wall breakwater and the pile breakwater is small in shallow water but it is great in deeper waters. The pile-supported vertical wall breakwater always gives smaller transmission and larger reflection than the curtain wall breakwater or the pile breakwater,

and its capability of energy dissipation becomes superior to that of the curtain wall or pile breakwater for longer waves.

Conclusions

Using the eigenfunction expansion method, a numerical model was developed that predicts various hydrodynamic characteristics of a pile-supported vertical wall breakwater. In order to examine the validity of the developed model, large-scale laboratory experiments were undertaken that involved regular or irregular waves of various wave characteristics impinging upon pile-supported vertical wall breakwaters having a constant spacing between piles but various drafts of the upper wall.

Comparisons between measurement and prediction showed that the numerical model was able to adequately reproduce most of the important features of the experimental results. For regular waves, the transmission coefficient decreased with the relative water depth, whereas the reflection coefficient and normalized wave force increased with the relative depth. On the other hand, as the relative depth increased, the normalized runup increased to a certain maximum value, and then decreased to unity as the relative depth further increased. As the draft of the upper wall increased, the transmission coefficient decreased, while the reflection coefficient and the normalized wave force increased, as expected. For the wave runup, the value of kh at which the maximum runup occurred became smaller as the draft of the upper wall increased.

For irregular waves, the numerical model somewhat over-predicted the frequency-averaged transmission and reflection coefficients and zero-moment wave force, especially at larger values. The effects of the relative water depth, draft of the upper wall, and peakedness of the spectrum on various frequency-averaged wave properties were examined. The effects of spectral peakedness were minimal. The frequency-averaged transmission coefficient decreased with the relative water depth, whereas the frequency-averaged reflection coefficient and zero-moment wave force increased with the relative depth. As the draft of the upper wall increased, the transmission coefficient decreased, while the reflection coefficient and wave force increased, as expected. Selected comparisons of measured and predicted wave and force spectra showed that the predicted spectra were in generally good agreement with the measured spectra.

Finally it was shown that the pile-supported vertical wall breakwater always gives

smaller transmission and larger reflection than a curtain wall breakwater or a pile breakwater and its capability of energy dissipation is superior to that of the curtain wall or pile breakwater for longer waves.

In the future, more investigations with different spacing between piles, different shape of piles such as circular piles, and obliquely incident waves may be necessary. The extension of the numerical model to a multiple-row pile-supported vertical wall breakwater and the associated laboratory experiments may also be necessary.

ACKNOWLEDGMENTS

KDS was supported by the Brain Korea 21 Project. The writers thank the assistance of Nathan Papini, who was supported as a Research Experience for Undergraduates (REU) student funded by the National Science Foundation (EEC-0244205). The writers also thank Terry Dibble and Christopher Scott of the O.H. Hinsdale Wave Research Laboratory for their assistance in conducting the experiments.

References

Bennett, G. S., McIver, P., and Smallman, J. V. (1992). "A mathematical model of a slotted wavescreen breakwater." *Coastal Engineering,* 18, 231-249.

Dean, R. G., and Dalrymple, R. A. (1991). *Water Wave Mechanics for Engineers and Scientists.* World Scientific, Singapore, 353 pp.

Goda, Y. (2000). *Random seas and design of maritime structures*. 2nd ed., World Scientific, Singapore, 443 pp.

Hagiwara, K. (1984). "Analysis of upright structure for wave dissipation using integral equation." *Proc., 19th Int. Conf. On Coastal Engineering (ICCE)*, ASCE, Reston, Va., 2810-2826.

Hayashi, T., Hattori, M., Kano, T., and Shirai, M. (1966). "Hydraulic research on the closely spaced pile breakwater." *Proc., 10th Int. Conf. on Coastal Engineering (ICCE)*, ASCE, Reston, Va., 873-884.

Isaacson, M., Premasiri, S., and Yang, G. (1998). "Wave interactions with vertical slotted barrier." *J. Waterw., Port, Coastal, Ocean Eng*., 124(3), 118-126.

Kakuno, S., and Liu, P. L.-F. (1993). "Scattering of water waves by vertical cylinders." *J.*

Waterw., Port, Coastal Ocean Eng., 119(4), 302-322.

Kim, B. H. (1998). "Interactions of waves, seabed and structures." PhD dissertation, Seoul National University, 246 pp.

Kojima, H., Utsunomiya, M., Ijima, T., Yoshida, A., and Kihara, T. (1988). "Analysis of hydraulic characteristics of permeable breakwaters to oblique incident waves." *Proc., 35th Japanese Conf. on Coastal Engineering*, Japan Society of Civil Engineers, 542-546 (in Japanese).

Kriebel, D. L. (2000). "Performance of vertical wave barriers in random seas." *Proc. Coastal Structures '99*, A. A. Balkema, Rotterdam, 525-532.

Kriebel, D. L., and Bollmann, C. A. (1996). "Wave transmission past vertical wave barriers." *Proc., 25th Int. Conf. on Coastal Engineering (ICCE)*, ASCE, Reston, Va., 2470-2483.

Kriebel, D., Sollitt, C., and Gerken, W. (1998). "Wave forces on a vertical wave barrier." *Proc., 26th Int. Conf. on Coastal Engineering (ICCE)*, ASCE, Reston, Va., 2069-2081.

Mei, C. C. (1983*). The Applied Dynamics of Ocean Surface Waves.* Wiley, New York, 740 pp.

Mei, C. C., Liu, P. L.-F., and Ippen, A. T. (1974). "Quadratic loss and scattering of long waves." *J. Waterw., Harbors, and Coastal Eng. Div.*, ASCE, 100(3), 217-239.

Park, W. S., Kim, B. H., Suh, K. D., and Lee, K. S. (2000). "Scattering of irregular waves by vertical cylinders*." Coastal Engineering Journal*, 42(2), 253-271.

Press, W. H., Teukolsky, S. A., Vetterling, W. T., and Flannery, B. P. (1992). *Numerical Recipes in FORTRAN: the Art of Scientific Computing*. Cambridge Univ. Press, Cambridge, 963 pp.

Suh, K. D., Park, W. S., and Park, B. S. (2001). "Separation of incident and reflected waves in wave-current flumes." *Coastal Engineering*, 43, 149-159.

Suh, K. D., Son, S. Y., Lee, J. I., and Lee, T. H. (2002). "Calculation of irregular wave reflection from perforated-wall caisson breakwaters using a regular wave model." *Proc., 28th Int. Conf. on Coastal Engineering (ICCE)*, ASCE, Reston, Va., 1709-1721.

Uda, T., Omata, A., and Kawamura, T. (1990). "An experimental study on wave dissipation and wave forces on the slit-type structures." *Rep. Public Works Res. Inst.,* 2891, Japan Ministry of Construction (in Japanese).

Wiegel, R. L. (1960). "Transmission of waves past a rigid vertical thin barrier." *J. Waterways and Harbors Div.*, ASCE, 86(WW1), 1-12.

Table 1. Summary of Experimental Results for Regular Waves

$\frac{d}{h}$	T (s)	H_i (cm)	C_t	C_r	$\frac{R_u^{(1)}}{H_i}$	$\frac{R_u^{(2)}}{H_i}$	$\frac{F_{\max}^{(1)}}{F_{S\max}}$	$\frac{F_{\max}^{(2)}}{F_{S\max}}$
(1)	(2)	(3)	(4)	(5)	(6)	(7)	(8)	(9)
0.2	1.48	9.5	0.36	0.93	1.07	1.06	0.83	0.80
0.2	1.99	17.6	0.62	0.63	0.87	0.84	0.44	0.43
0.2	2.50	25.1	0.82	0.38	0.77	0.75	0.28	0.26
0.2	2.99	32.2	0.81	0.23	0.75	0.68	0.23	0.20
0.2	4.01	47.0	0.88	0.14	0.84	0.70	0.21	0.17
0.4	1.48	10.1	0.14	1.00	1.16	1.10	1.11	1.13
0.4	1.98	16.7	0.27	0.93	1.15	1.12	0.83	0.82
0.4	2.51	24.7	0.55	0.67	1.07	1.04	0.60	0.59
0.4	2.99	32.7	0.64	0.41	0.90	0.87	0.44	0.41
0.4	4.00	48.6	0.72	0.35	1.06	0.88	0.45	0.36
0.6	1.48	9.8	0.16	1.00	1.16	1.09	1.00	1.16
0.6	1.98	16.7	0.11	0.99	1.12	1.04	0.90	0.92
0.6	2.51	25.9	0.28	0.83	1.03	0.98	0.77	0.76
0.6	2.99	32.4	0.44	0.65	0.97	0.93	0.66	0.62
0.6	3.99	41.1	0.55	0.49	1.01	0.88	0.61	0.52

Table 2. Summary of Experimental Results for Irregular Waves

$\frac{d}{h}$	γ	T_p (s)	H_s (cm)	$k_p h$	$\frac{H_s}{L_p}$	$\overline{C}_t^m$	$\overline{C}_t^p$	$\overline{C}_r^m$	$\overline{C}_r^p$	$\hat{F}_{mo}^m$	$\hat{F}_{mo}^p$
(1)	(2)	(3)	(4)	(5)	(6)	(7)	(8)	(9)	(10)	(11)	(12)
0.2	3.3	1.72	10.9	3.24	0.024	0.33	0.29	0.85	0.95	0.41	0.52
0.2	3.3	2.18	19.7	2.10	0.027	0.54	0.56	0.70	0.80	0.31	0.39
0.2	3.3	2.59	24.4	1.58	0.025	0.70	0.75	0.57	0.60	0.23	0.28
0.2	3.3	2.96	38.6	1.29	0.033	0.71	0.80	0.49	0.50	0.20	0.23
0.2	3.3	3.75	49.7	0.93	0.031	0.75	0.86	0.38	0.37	0.15	0.16
0.4	3.3	1.68	9.5	3.43	0.022	0.18	0.15	0.92	0.99	0.57	0.66
0.4	3.3	2.16	18.6	2.12	0.026	0.28	0.27	0.87	0.95	0.50	0.61
0.4	3.3	2.62	24.1	1.55	0.025	0.46	0.49	0.76	0.84	0.44	0.53
0.4	3.3	3.09	35.3	1.20	0.028	0.57	0.64	0.61	0.70	0.34	0.44
0.4	3.3	3.86	49.6	0.90	0.030	0.63	0.76	0.52	0.53	0.28	0.33
0.6	3.3	1.79	11.6	3.04	0.023	0.12	0.09	0.90	1.00	0.59	0.70
0.6	3.3	2.38	21.0	1.80	0.025	0.12	0.16	0.91	0.98	0.54	0.65
0.6	3.3	2.73	27.1	1.45	0.026	0.25	0.29	0.84	0.94	0.55	0.66
0.6	3.3	3.04	34.8	1.23	0.029	0.37	0.43	0.76	0.87	0.51	0.63
0.6	3.3	3.62	49.8	0.97	0.032	0.45	0.57	0.67	0.74	0.44	0.54
0.4	1.0	1.69	9.2	3.39	0.021	0.16	0.13	0.90	0.99	0.55	0.64
0.4	1.0	2.21	17.2	2.04	0.023	0.27	0.28	0.85	0.95	0.46	0.56
0.4	1.0	2.70	25.0	1.46	0.024	0.45	0.46	0.77	0.86	0.39	0.49
0.4	1.0	3.13	33.1	1.19	0.026	0.51	0.59	0.69	0.76	0.34	0.43
0.4	1.0	3.92	47.3	0.88	0.028	0.60	0.73	0.54	0.58	0.28	0.34
0.4	10.0	1.63	9.4	3.65	0.023	0.21	0.11	0.93	0.99	0.63	0.72
0.4	10.0	2.12	18.4	2.19	0.027	0.28	0.26	0.88	0.96	0.52	0.65
0.4	10.0	2.62	27.3	1.54	0.028	0.50	0.52	0.73	0.82	0.45	0.55
0.4	10.0	3.01	33.2	1.25	0.028	0.60	0.68	0.54	0.66	0.35	0.45
0.4	10.0	3.86	46.6	0.90	0.028	0.64	0.80	0.48	0.46	0.29	0.31

Caption of figures

1. Definition sketch: (a) side view; (b) front view
2. Sketch of wave flume and experimental setup: (a) side view; (b) top view. WG = wave gauge, RG = runup wave gauge, LC = load cell
3. Lee side view of breakwater model attached to sidewalls by four load cells
4. Comparison of predicted hydrodynamic coefficients with experimental results as function of kh for various drafts of upper wall: (a) transmission coefficient; (b) reflection coefficient; (c) energy loss coefficient. Predicted: (——) $d/h = 0.2$, (- - -) $d/h = 0.4$, (– · – · –) $d/h = 0.6$. Measured: (○) $d/h = 0.2$, (□) $d/h = 0.4$, (△) $d/h = 0.6$
5. Comparison of predicted runup with experimental results as function of kh for various drafts of upper wall: (a) runup = maximum height of water level above still water level at breakwater; (b) runup = one half of vertical distance between wave crest and trough at breakwater. Predicted: (——) $d/h = 0.2$, (- - -) $d/h = 0.4$, (……) $d/h = 0.6$. Measured: (○) $d/h = 0.2$, (□) $d/h = 0.4$, (△) $d/h = 0.6$
6. Comparison of predicted wave force with experimental results as function of kh for various drafts of upper wall. Predicted: (——) $d/h = 0.2$, (- - -) $d/h = 0.4$, (……) $d/h = 0.6$. Measured: (○) $d/h = 0.2$, (□) $d/h = 0.4$, (△) $d/h = 0.6$
7. Comparison of frequency-averaged transmission coefficient between measurement and prediction
8. Comparison of frequency-averaged reflection coefficient between measurement and prediction
9. Comparison of dimensionless zero-moment force between measurement and prediction
10. Comparison of predicted hydrodynamic coefficients and wave force with experimental results as function of $k_p h$ for various drafts of upper wall: (a) frequency-averaged transmission coefficient; (b) frequency-averaged reflection coefficient; (c) dimensionless zero-moment force. Predicted: (——) $d/h = 0.2$, (- - -) $d/h = 0.4$, (……) $d/h = 0.6$. Measured: (○) $d/h = 0.2$, (□) $d/h = 0.4$, (△) $d/h = 0.6$
11. Comparison of predicted hydrodynamic coefficients and wave force with

experimental results as function of $k_p h$ for various values of peak enhancement factor: (a) frequency-averaged transmission coefficient; (b) frequency-averaged reflection coefficient; (c) dimensionless zero-moment force. Predicted: (——) $\gamma = 1.0$, (- - -) $\gamma = 3.3$, (……) $\gamma = 10.0$. Measured: (○) $\gamma = 1.0$, (□) $\gamma = 3.3$, (△) $\gamma = 10.0$

12. Measured (solid line) and predicted (dashed line) spectra for broad incident wave spectrum with $\gamma = 1.0$, T_p = 2.7 s, H_s = 25.0 cm, and d/h = 0.4: (a) incident wave; (b) transmitted wave; (c) reflected wave; (d) wave force
13. Measured (solid line) and predicted (dashed line) spectra for ordinary incident wave spectrum with $\gamma = 3.3$, T_p = 2.62 s, H_s = 24.1 cm, and d/h = 0.4: (a) incident wave; (b) transmitted wave; (c) reflected wave; (d) wave force
14. Measured (solid line) and predicted (dashed line) spectra for narrow incident wave spectrum with $\gamma = 10.0$, T_p = 2.62 s, H_s = 27.3 cm, and d/h = 0.4: (a) incident wave; (b) transmitted wave; (c) reflected wave; (d) wave force
15. Measured (solid line) and predicted (dashed line) spectra for case of smallest average error of numerical model with $d/h = 0.2$, $\gamma = 3.3$, T_p = 3.75 s, and H_s = 49.7 cm: (a) incident wave; (b) transmitted wave; (c) reflected wave; (d) wave force
16. Measured (solid line) and predicted (dashed line) spectra for case of greatest average error of numerical model with $d/h = 0.4$, $\gamma = 10.0$, T_p = 1.63 s, and H_s = 9.4 cm: (a) incident wave; (b) transmitted wave; (c) reflected wave; (d) wave force
17. Comparison of hydrodynamic coefficients of various breakwaters as function of $k_p h$: (a) frequency-averaged transmission coefficient; (b) frequency-averaged reflection coefficient; (c) frequency-averaged energy loss coefficient. (——) pile-supported vertical wall breakwater, (- - -) curtain wall breakwater, (……) pile breakwater

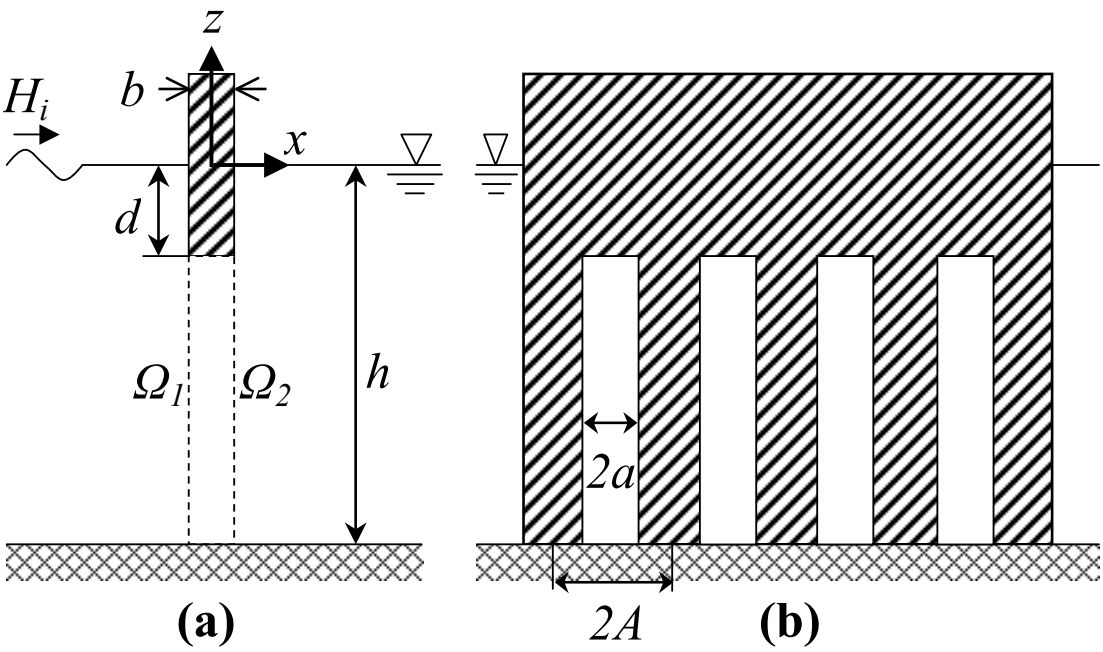

Fig. 1 Definition sketch: (a) side view; (b) front view

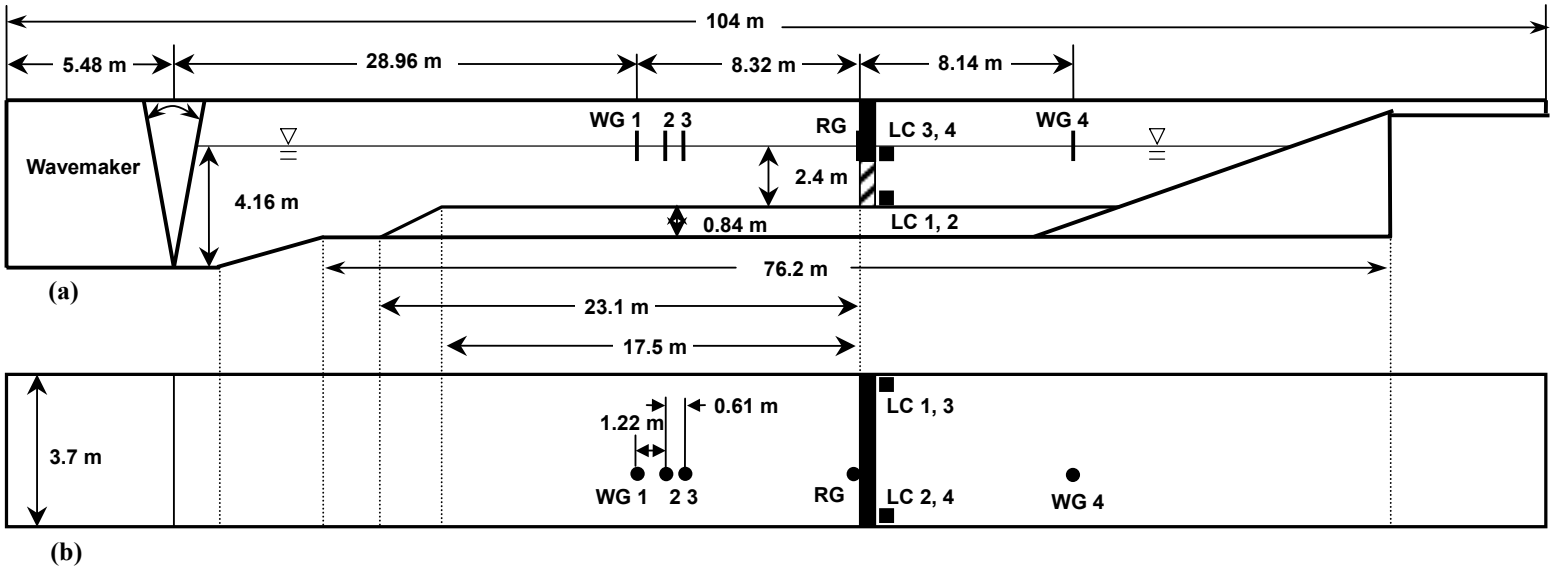

Fig. 2 Sketch of wave flume and experimental setup: (a) side view; (b) top view. WG = wave gauge, RG = runup wave gauge, LC = load cell

Fig. 3 Lee side view of breakwater model attached to sidewalls by four load cells

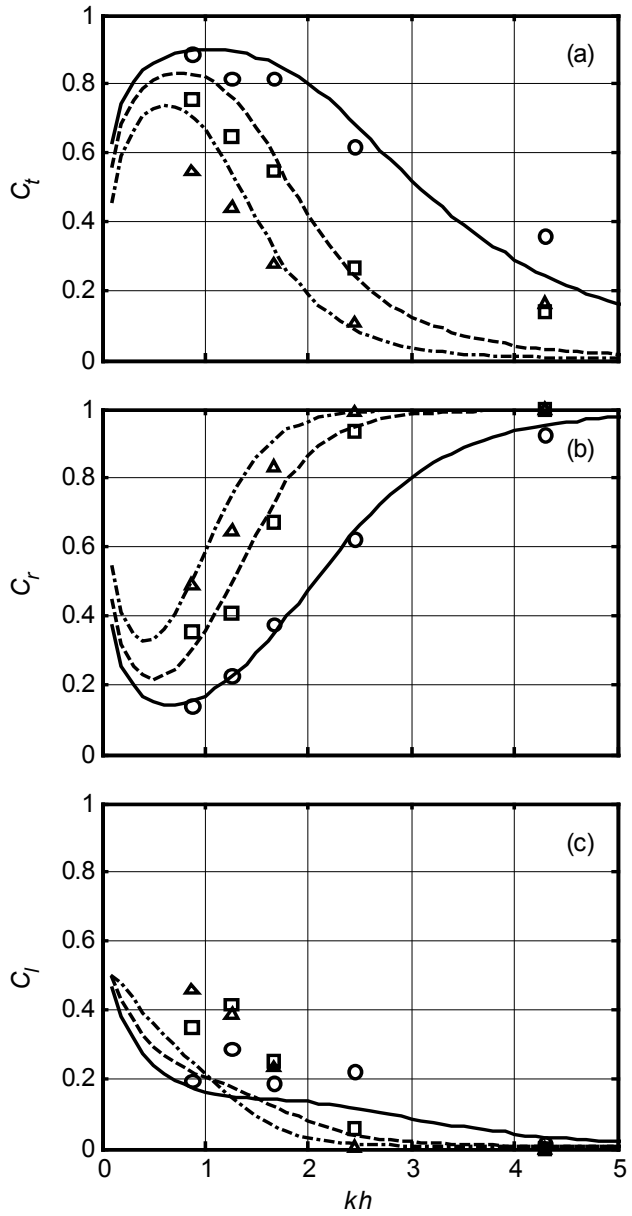

Fig. 4 Comparison of predicted hydrodynamic coefficients with experimental results as function of kh for various drafts of upper wall: (a) transmission coefficient; (b) reflection coefficient; (c) energy loss coefficient. Predicted: (——) $d/h = 0.2$, (— — —) $d/h = 0.4$, (— · — · —) $d/h = 0.6$. Measured: (○) $d/h = 0.2$, (□) $d/h = 0.4$, (△) $d/h = 0.6$

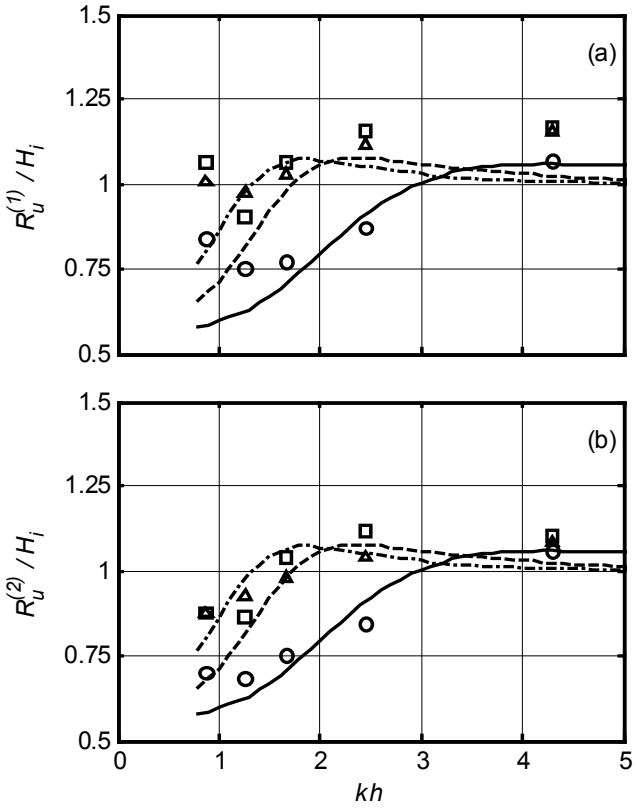

Fig. 5 Comparison of predicted runup with experimental results as function of kh for various drafts of upper wall: (a) runup = maximum height of water level above still water level at breakwater; (b) runup = one half of vertical distance between wave crest and trough at breakwater. Predicted: (——) $d/h = 0.2$, **(— — —)** $d/h = 0.4$, **(— · — · —)** $d/h = 0.6$. Measured: (○) $d/h = 0.2$, (□) $d/h = 0.4$, (△) $d/h = 0.6$

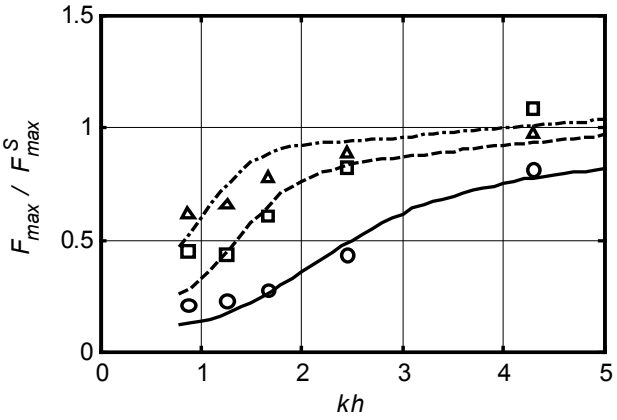

Fig. 6 Comparison of predicted wave force with experimental results as function of kh for various drafts of upper wall. Predicted: (——) $d/h = 0.2$, (— — —) $d/h = 0.4$, (— · — · —) $d/h = 0.6$. Measured: (○) $d/h = 0.2$, (□) $d/h = 0.4$, (△) $d/h = 0.6$

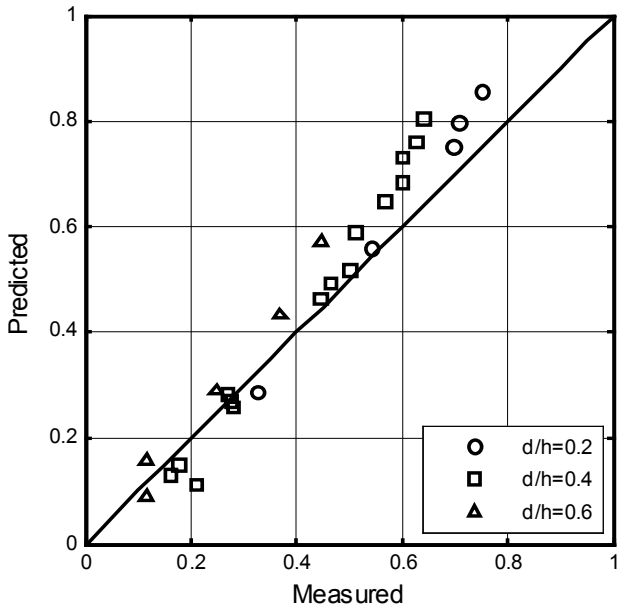

Fig. 7 Comparison of frequency-averaged transmission coefficient between measurement and prediction

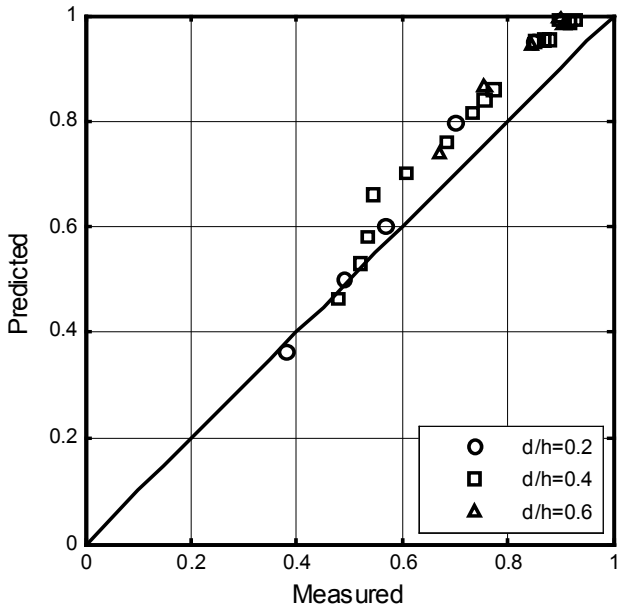

Fig. 8 Comparison of frequency-averaged reflection coefficient between measurement and prediction

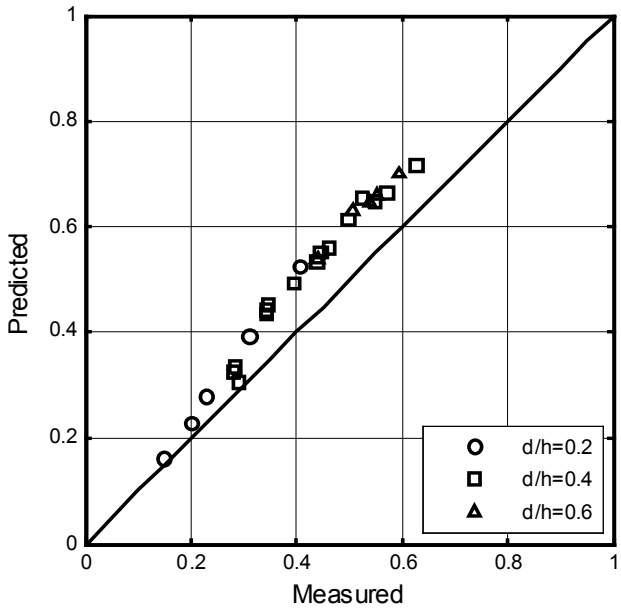

Fig. 9 Comparison of dimensionless zero-moment force between measurement and prediction

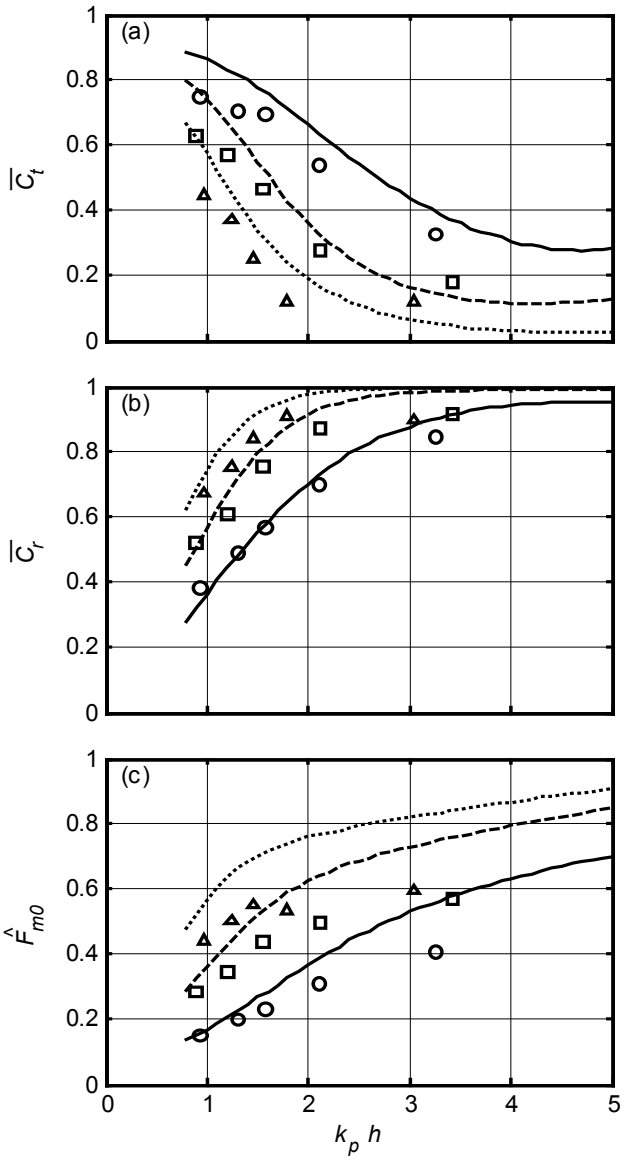

Fig. 10 Comparison of predicted hydrodynamic coefficients and wave force with experimental results as function of $k_p h$ for various drafts of upper wall: (a) frequency-averaged transmission coefficient; (b) frequency-averaged reflection coefficient; (c) dimensionless zero-moment force. Predicted: (——) $d/h = 0.2$, (— — —) $d/h = 0.4$, (……) $d/h = 0.6$. Measured: (○) $d/h = 0.2$, (□) $d/h = 0.4$, (△) $d/h = 0.6$

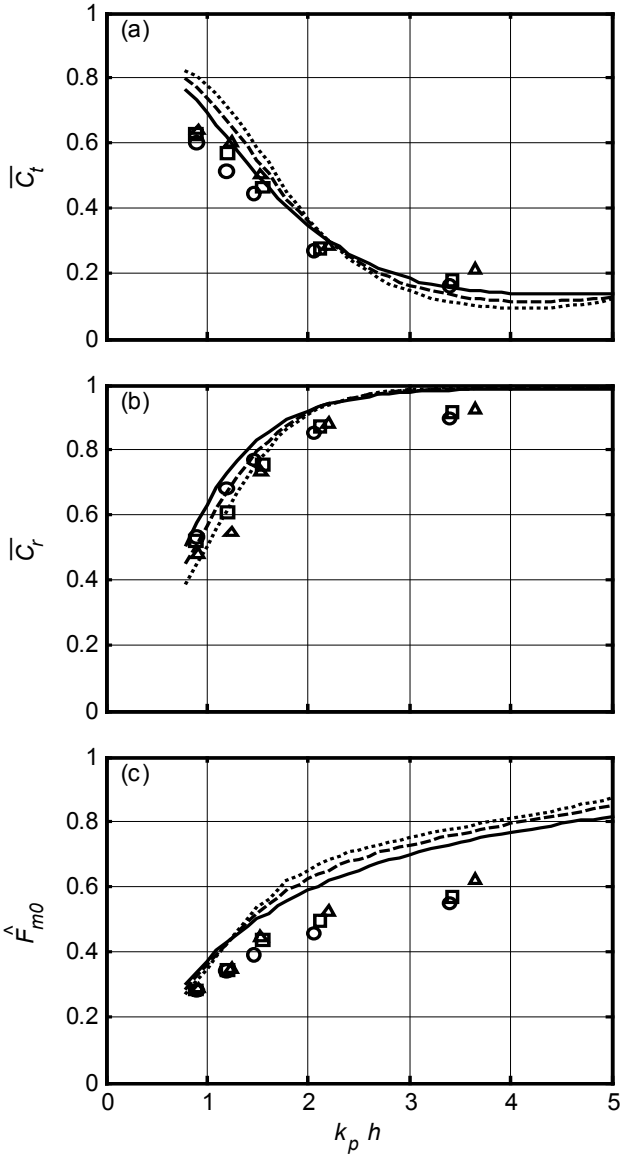

Fig. 11 Comparison of predicted hydrodynamic coefficients and wave force with experimental results as function of $k_p h$ for various values of peak enhancement factor: (a) frequency-averaged transmission coefficient; (b) frequency-averaged reflection coefficient; (c) dimensionless zero-moment force. Predicted: (——) $\gamma = 1.0$, (— — —) $\gamma = 3.3$, (……) $\gamma = 10.0$. Measured: (○) $\gamma = 1.0$, (□) $\gamma = 3.3$, (△) $\gamma = 10.0$

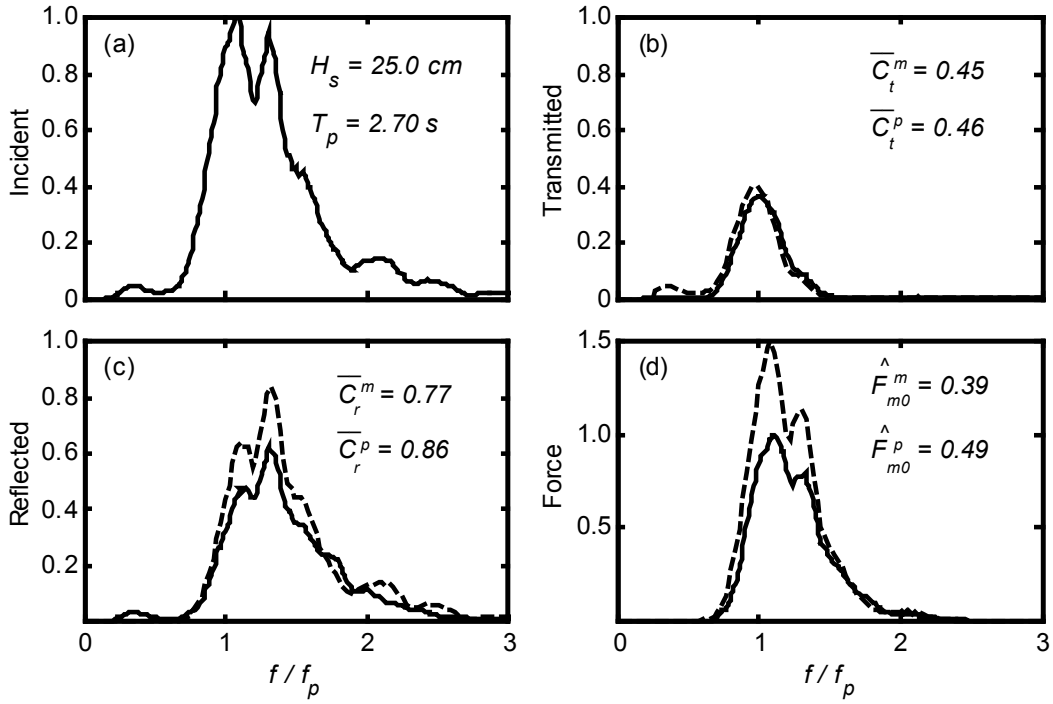

Fig. 12 Measured (solid line) and predicted (dashed line) spectra for broad incident wave spectrum with $\gamma = 1.0$, $T_p = 2.7$ s, $H_s = 25.0$ cm, and $d/h = 0.4$: (a) incident wave; (b) transmitted wave; (c) reflected wave; (d) wave force

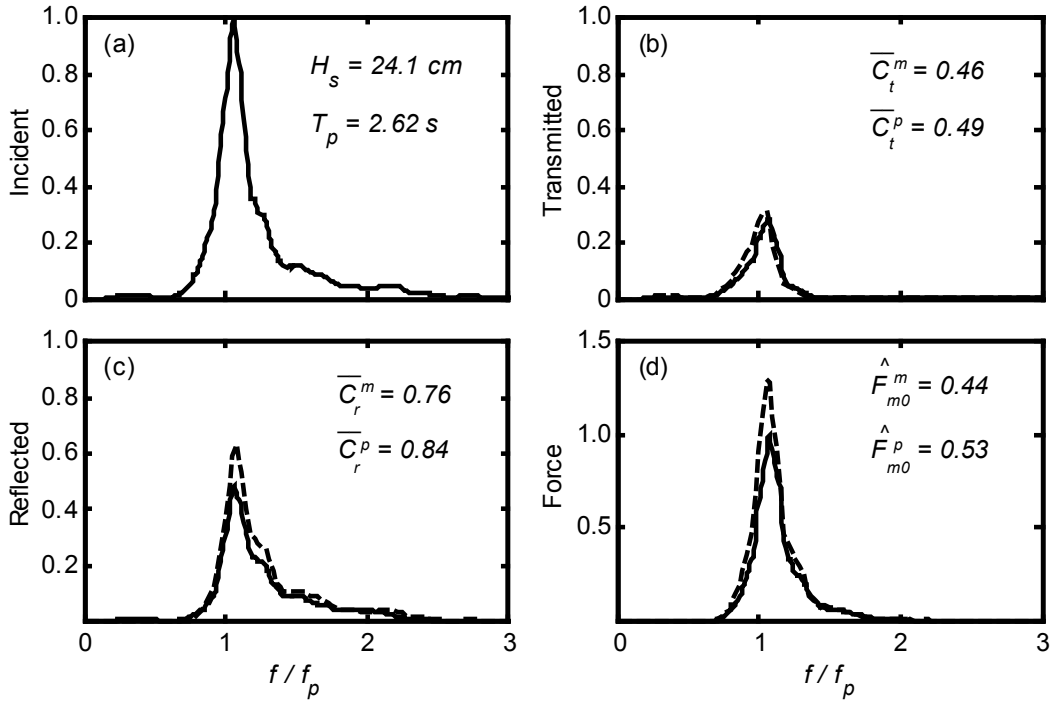

Fig. 13 Measured (solid line) and predicted (dashed line) spectra for ordinary incident wave spectrum with $\gamma = 3.3$, T_p = 2.62 s, H_s = 24.1 cm, and d/h = 0.4: (a) incident wave; (b) transmitted wave; (c) reflected wave; (d) wave force

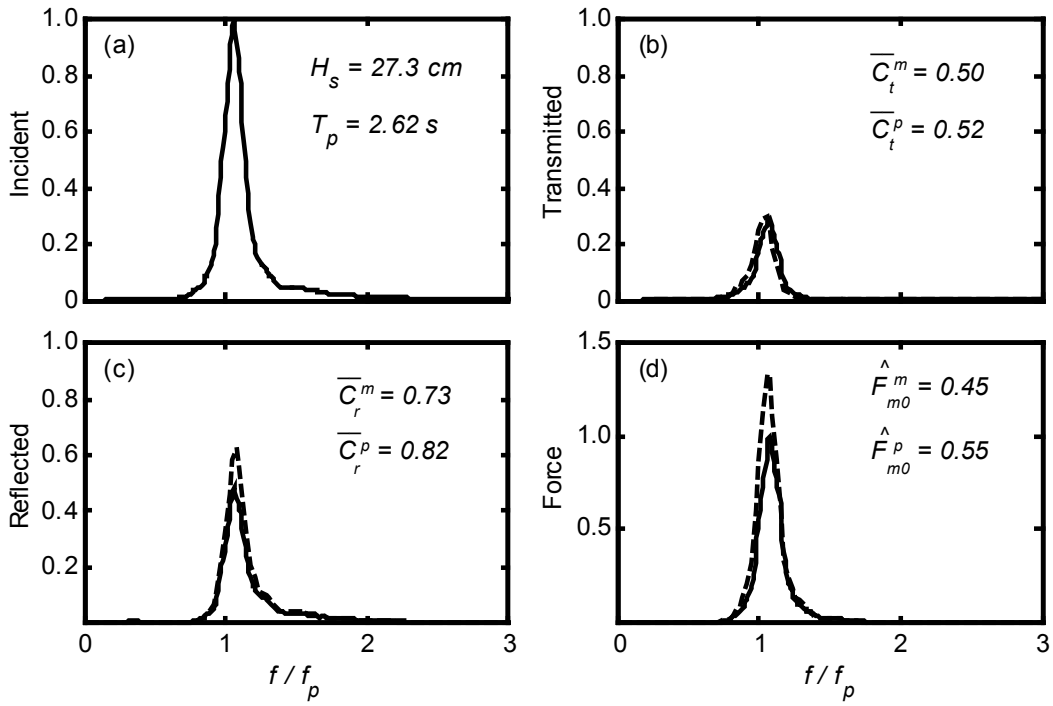

Fig. 14 Measured (solid line) and predicted (dashed line) spectra for narrow incident wave spectrum with $\gamma = 10.0$, T_p = 2.62 s, H_s = 27.3 cm, and d/h = 0.4: (a) incident wave; (b) transmitted wave; (c) reflected wave; (d) wave force

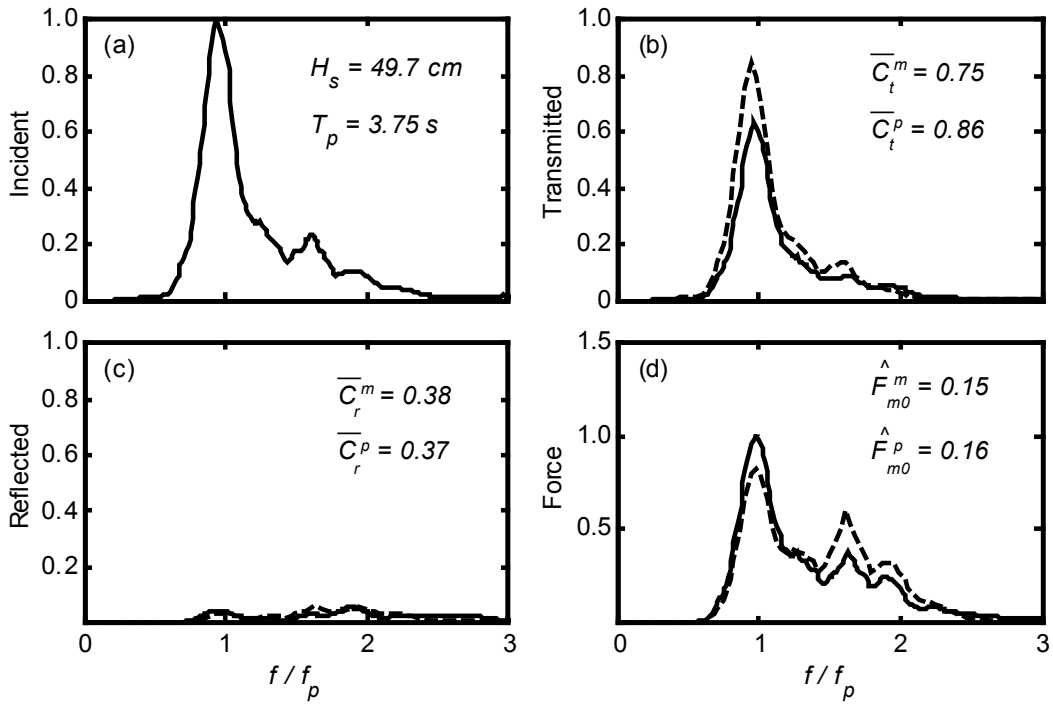

Fig. 15 Measured (solid line) and predicted (dashed line) spectra for case of smallest average error of numerical model with $d/h = 0.2$, $\gamma = 3.3$, T_p = 3.75 s, and H_s = 49.7 cm: (a) incident wave; (b) transmitted wave; (c) reflected wave; (d) wave force

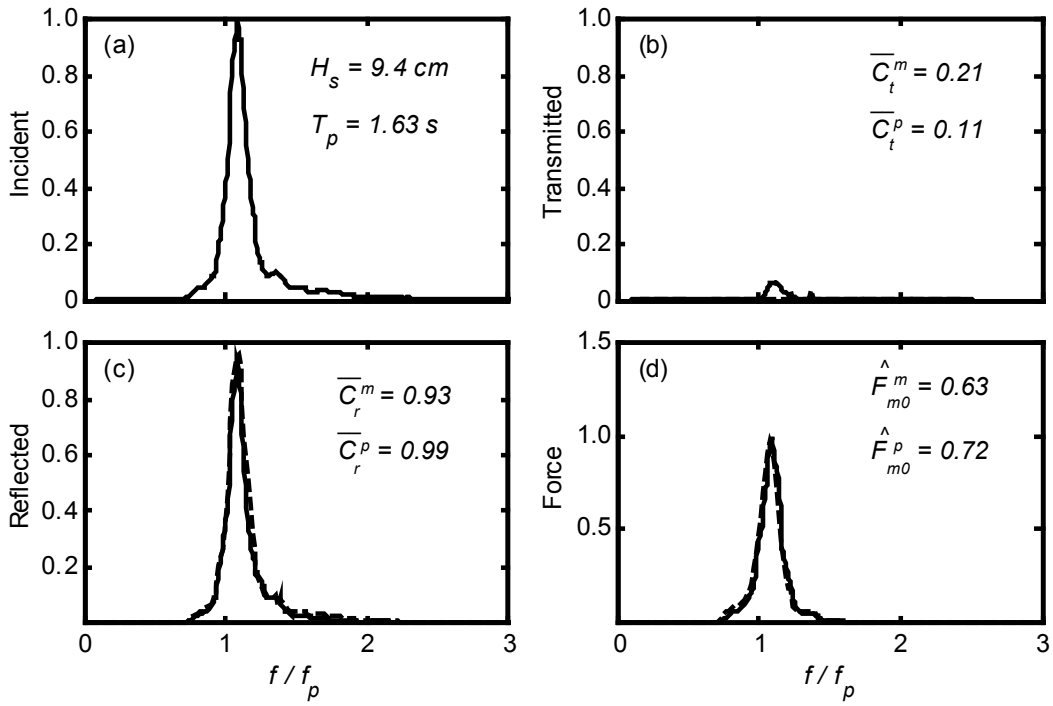

Fig. 16 Measured (solid line) and predicted (dashed line) spectra for case of greatest average error of numerical model with $d/h = 0.4$, $\gamma = 10.0$, T_p = 1.63 s, and H_s = 9.4 cm: (a) incident wave; (b) transmitted wave; (c) reflected wave; (d) wave force

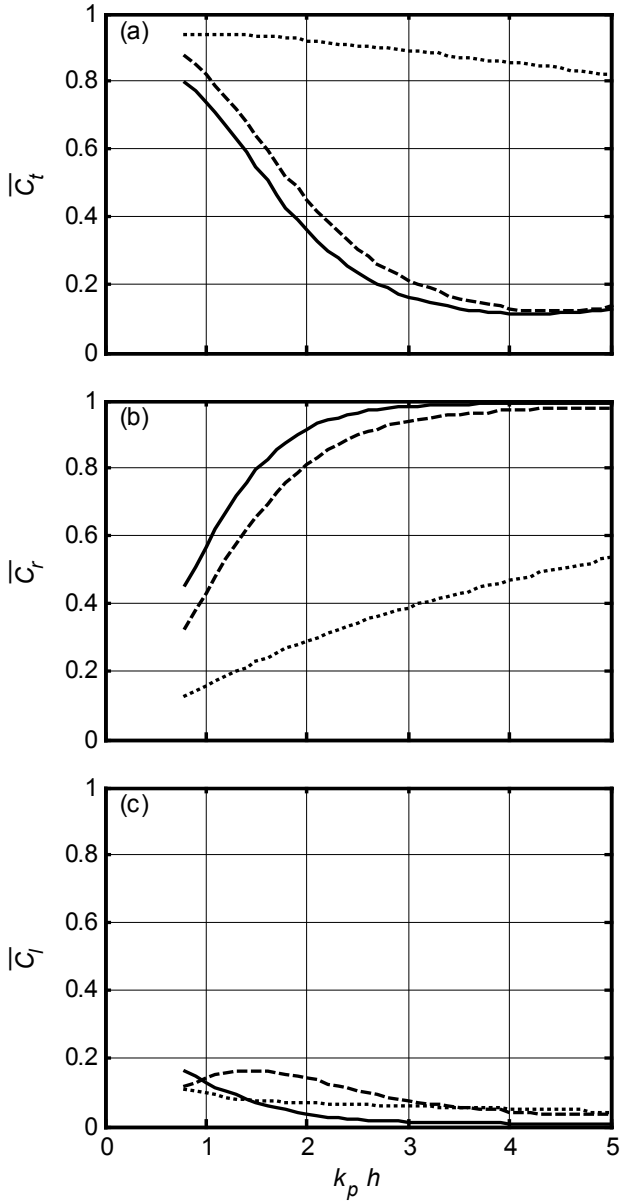

Fig. 17 Comparison of hydrodynamic coefficients of various breakwaters as function of $k_p h$: (a) frequency-averaged transmission coefficient; (b) frequency-averaged reflection coefficient; (c) frequency-averaged energy loss coefficient. (——) pile-supported vertical wall breakwater, (— — —) curtain wall breakwater, (……) pile breakwater